Md Ibrahim Khalil
Department of Mechanical Engineering,
University of Maine,
Orono, ME 04473
e-mail: md.khalil@maine.edu

Dezhong Tong
Department of Mechanical and
Aerospace Engineering,
University of California, Los Angeles,
Los Angeles, CA 90095
e-mail: tltl960308@ucla.edu

Guanjin Wang
Department of Mechanical and
Aerospace Engineering,
University of California, Los Angeles,
Los Angeles, CA 90095
e-mail: gjwang@g.ucla.edu

Mohammad Khalid Jawed[1]
Assistant Professor
Department of Mechanical and
Aerospace Engineering,
University of California, Los Angeles,
Los Angeles, CA 90095
e-mail: khalidjm@seas.ucla.edu

Bashir Khoda[1]
Assistant Professor
Department of Mechanical Engineering,
University of Maine,
Orono, ME 04473
e-mail: bashir.khoda@maine.edu

Systematic Variation of Friction of Rods

The mechanical response of a knot tied in elastic rods strongly depends on the frictional force due to rod–rod contact. The behavior of a knot can be qualitatively different based on the frictional coefficient of the elastic rod. Systematic variation of friction during rod–rod contact is a crucial component of any experimental design to uncover the underlying ingredients behind the mechanics of knots. In this paper, we demonstrate a novel process of controlling the friction of a continuous rod by adhering non-spherical inorganic micro-particles. Polymeric binder is used to deliver the particles as asperities over the rod substrate and by controlling their size and distribution the coefficient of friction of the rod is determined. In parallel, numerical simulations with the discrete elastic rods algorithm are used to reproduce the experimental observations. Tabletop experiments are performed where overhand knots with a variety of unknotting numbers are pulled tight. The force–extension curve of these experiments shows that the proposed process can successfully tune the friction between rods. [DOI: 10.1115/1.4055544]

Keywords: computational mechanics, elasticity, mechanical properties of materials

1 Introduction

We use knots in ropes everyday for sailing, fishing, climbing, surgical procedures, and various industrial applications. The Ashley Book of Knots contains illustrations on more than 3800 different types of knots [1], each with a different topology. A knot almost invariably involves frictional contact between rods except extremely rare cases [2]. In addition to the topology, the mechanical response of a knot is governed by the frictional coefficient of the contact [3]. Overall, the mechanics of a knot is a function of its topology, friction, and material parameters. This leads to a highly coupled system with fascinating mechanical behavior. Examples abound in our everyday life. When tying shoelace knots, mistakenly tying the "granny" knot instead of the "reef" knot can dramatically decrease its performance, i.e., the knot may get undone at a small amount of external force. Knots can even serve as a "topological battery" where a number of tangled rods remain tangled without any external force or boundary conditions and keep elastic strain energy stored within it [4].

Due to the rich—and often physically non-intuitive—mechanical behavior of knots and tangles, researchers have explored their mechanics using theory [5], simulations [6–10], and experiments [3,11]. Modeling of friction in theories and simulations usually relies on heuristic observations, e.g., Coulomb's law of friction. Systematic experiments can help uncover the role of various ingredients—topology, friction, and material stiffness—on the mechanics of knots. Jawed et al. [3] varied the topology of overhand knots and explored the force required to pull the knots tight. Patil et al. [11] used knotted fibers that change their color upon material deformation and analyzed the mechanics of a few commonly used knots. To the best of our knowledge, none of these prior works used the coefficient of friction as a control parameter despite its critical role in determining the strength of a knot [3]. This paper addresses the critical challenge of systematically varying the friction coefficient of rods by welding asperities to the outer surface of otherwise smooth elastomeric rods.

Various particle delivery techniques are available at different operating conditions. Vacuum deposition techniques like physical vapor deposition [12,13], chemical vapor deposition [14,15], or plasma sputtering [16,17] methods are generally applied for thin and uniform deposition of metallic layers in low to high vacuum conditions, which makes them slow, arduous, and expensive at industrial scale. For example, a nickel–phosphorus (Ni–P) thin-film through electroless plating is reported a uniform 64 μm thickness with 6 h of operation time [18]. In contrast, solution or sol–gel coating methods [19] (i.e., dip coating, spin coating, spray coating, roll coating, blade coating, and Langmuir–Blodgett) can be applied in atmospheric conditions where the solution evaporates and makes a dried thin-film [20–22].

Dip coating is a wet deposition method by immersion of the substrate into a solution, mixture, or collide. It is an effective and straightforward way of thin-film/layers formation of pure liquid or hydrolyzable metal compounds or readily formed particles. It is

[1]Corresponding authors.

Contributed by the Applied Mechanics Division of ASME for publication in the Journal of Applied Mechanics. Manuscript received June 2, 2022; final manuscript received August 30, 2022; published online September 27, 2022. Assoc. Editor: Yong Zhu.

extensively used as a coating method due to its simplicity, low cost, and reasonable control over the thickness. The mixtures are often embedded with inorganic fillers, nanoparticles, or clusters ($d <$ 30 nm) that produce thin-film impregnated particles ranging from nanometer to couple microns. Such coat of pure-polymer or impregnated nanoparticles acts as lubricant [23] and creates abrasion-resistance coating for many applications including orthodontic wires [24], guidewires for angiography and interventional procedures, self-lubricated coronaresistant electrical wire [25], anti-icing surface [26], super hydrophilic or olio-phobic surface, etc.

In previous studies, four parameters (coating-to-substrate hardness relationship, thickness of the coating, surface roughness, and size and hardness of debris in the contact) have been mentioned that control the friction in the tribological contact process [27]. Particles are transferred in the interface of the substrate while withdrawing from the suspension [28,29]. The efficiency of particle transfer is dictated by the competition between the capillary force and viscous drag force during the withdrawal of the substrate [30]. The thickness of the material transfer over a flat plate can be determined by the famous Landau–Levich–Derjaguin (LLD) equation [31,32] which is $h = 0.94\ L_c\ Ca^{2/3}$. Here, $L_c = \sqrt{\gamma/\rho g}$ is the capillary length and $Ca = \eta U/\gamma$ is the capillary number; γ and η are the surface tension and the viscosity of the suspension, U is the withdrawal speed of the substrate, and g is the acceleration with respect to gravity. The modified LLD equation for the cylindrical substrate is expressed as $h = 1.34\ r\ Ca^{2/3}$ which is used to predict the material transfer over the wires and fibers [33]. This film formation technique over the substrate is widely used in various industrial applications such as modification of cutting tools [34], corrosion protective layer [35], biosensors [36], particle filtration [37,38], and joining of the metal lattice structure produced with continuous thin rod [39,40].

The aim of this work is to observe the mechanical response of the knots by the variation of the friction force. The comparison of the snapshots of the shape of the knots of experiment and simulation at six different positions are presented in Fig. 1. Non-spherical irregular edge shaped particles are entrained over the elastic rods which subject to introduce the asperities. The asperities over the elastic rods result in increase in friction forces. Thus, the friction force is controlled by controlling the particle adherence over the substrate during the coating process. Moreover, the coefficient of friction is determined by fitting the experimental results with the simulation results.

2 Problem Statement

The overhand knot tying process with varying friction coefficients was employed to demonstrate the effectiveness of the simulation framework. Then the computational framework was extended to investigate the sensitive dependence of the snap-through instability on the friction during rod–rod contact.

2.1 Simulations by Discrete Elastic Rods. The computational framework, based on discrete elastic rods (DERs) [41,42], recently proposed in Ref. [9] was adopted and extended in this work for simulating knots with a systematic variation of frictional contact. DER, as a discrete-differential-geometry-based framework [43], was first introduced by the computer science community and is becoming progressively attractive to engineering disciplines for its high accuracy and low computational cost across various physical scenarios, i.e., coiling patterns on the moving substrate [44], buckling of rotating flagella [45], grid shells [46], etc.

In DER, as shown in Fig. 2(*a*), an elastic rod will be discretized into $N+1$ nodes $\mathbf{x}_i$, where i is in the range from 0 to N, and N edges $\mathbf{e}^i = \mathbf{x}_{i+1} - \mathbf{x}i$. Subscripts are used for quantities associated with nodes and superscripts for those with edges. Each edge $\mathbf{e}_i$ is attached with two orthogonal frames: reference frame $[\mathbf{t}^i, \mathbf{d}_1^i, \mathbf{d}_2^i]$ and material frame $[\mathbf{t}^i, \mathbf{m}_1^i, \mathbf{m}_2^i]$. The reference frame is predefined at initial time $t = 0\ s$, and the material frame can be obtained based on the reference frame with a rotation angle θ^i. $3N+3$ nodal positions and N rotation angles can constitute the vector of a $4N+3$ degrees-of-freedom:

$$\mathbf{q} = \left[\mathbf{x}_0, \theta^0, \mathbf{x}_1, \theta^1, \ldots, \mathbf{x}_{N-1}, \theta^{N-1}, \mathbf{x}_N\right]^T \tag{1}$$

The equations of motion (EOM) can be constructed by the elastic energies of the rod, such as stretching, bending, and twisting energy, as well as external forces, like contact and friction, represented by the generalized coordinate in Eq. (1). Specifically, the stretching energy is defined as

$$E_i^s = \sum_{i=0}^{n-1} \frac{1}{2} EA \left(1 - \frac{\|\mathbf{e}_i\|}{\|\bar{\mathbf{e}}_i\|}\right)^2 \|\bar{\mathbf{e}}_i\| \tag{2}$$

where EA is the stretching stiffness, E is the Young's modulus, A is the cross-sectional area, and $\bar{\mathbf{e}}_i$ is the undeformed edge. Hereafter, all quantities with a bar mean the quantities under undeformed status. Next, the bending energy is written as

$$E_i^b = \sum_{i=1}^{n-1} \frac{1}{2} \frac{EI}{\|\bar{\mathbf{e}}_i\|} \left(2 \tan\frac{\phi_i}{2} - 2 \tan\frac{\bar{\phi}_i}{2}\right)^2 \tag{3}$$

where EI is the bending stiffness, $I = \pi r_0^4/4$ is the moment of inertia, r_0 is the rod radius, and ϕ_i is the turning angle which is shown in Fig. 2(*b*). After that, the twisting energy is defined as follows:

$$E_i^t = \sum_{i=2}^{n} \frac{1}{2} \frac{GJ}{\|\bar{\mathbf{e}}_i\|} (\tau_i - \bar{\tau}_i)^2 \tag{4}$$

where GJ is the twisting stiffness, $G = E/2(1+\nu)$ is the shear modulus, ν is the Poisson's ratio, $J = \pi r_0^4/2$ is the polar second moment of inertia, $\tau_i = \theta_{i+1} - \theta_i + \Delta\tau^{\text{ref}}$ is the discrete twist at

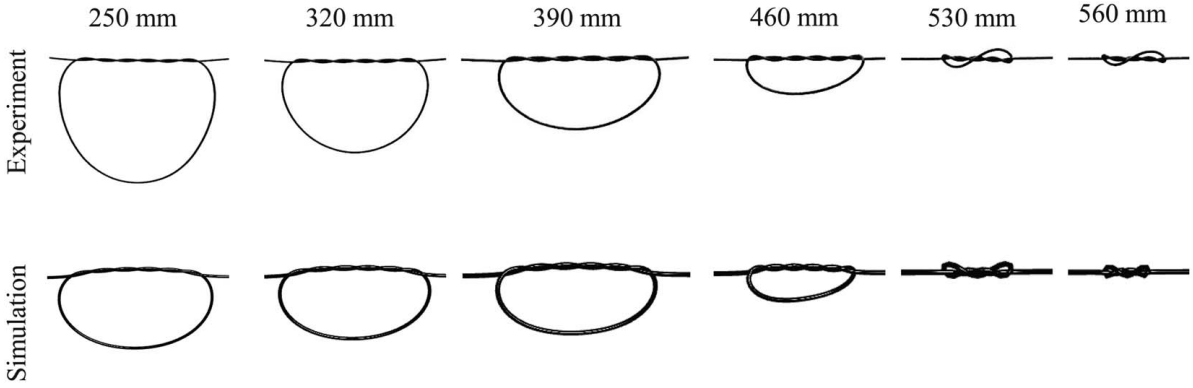

Fig. 1 Comparison of the shape of the knots in both experiment and simulation at six different positions. The uncoated rod at $n = 3$ is used for the comparison and initially, the end-to-end length is 250 mm for both experiment and simulation.

node $\mathbf{q}_i$, and $\Delta\tau^{\text{ref}}$ is the discrete reference twist. Then the internal force of the ith node $\mathbf{F}_i^{\text{int}}$ is defined in terms of energy as

$$\mathbf{F}_i^{\text{int}} = \frac{\partial(E_i^s + E_i^b + E_i^t)}{\partial \mathbf{q}_i} \tag{5}$$

With that, the EOM for the system is written as

$$\mathbf{M}\ddot{\mathbf{q}} - \mathbf{F}^{\text{int}} - \mathbf{F}^{\text{ext}} = 0 \tag{6}$$

In the DER algorithm, the implicit Euler method is implemented for time integration of the EOM, updating the status of $\mathbf{q}$ from t_{old} to $t_{\text{new}} + \Delta t$. Hereafter, all quantities with the subscript "new" mean that status is unknown, and quantities associated with the subscript "old" are known. Then, EOM is formulated as

$$f(\mathbf{q}_{\text{new}}) = \frac{\mathbb{M}}{\Delta t}\left(\frac{\mathbf{q}_{\text{new}} - \mathbf{q}_{\text{old}}}{\Delta t} - \dot{\mathbf{q}}_{\text{old}}\right) - \mathbf{F}_{\text{new}}^{\text{int}} - \mathbf{F}_{\text{new}}^{\text{ext}} = 0 \tag{7}$$

where $\mathbf{F}_{\text{new}}^{\text{int}}$ is defined as

$$\mathbf{F}_{\text{new}}^{\text{int}} = \frac{\partial(E_s + E_b + E_t)_{\text{new}}}{\partial \mathbf{q}_{\text{new}}} \tag{8}$$

In Eq. (7), $\mathbb{M}$ is the diagonal mass matrix (size is $4N + 3 \times 4N + 3$), $\mathbf{F}^{\text{int}}$ are the elastic forces, and $\mathbf{F}^{\text{ext}}$ are the external forces. $\dot{(\cdot)}$ stands for the derivative via time. In the knot tying case, $\mathbf{F}^{\text{ext}}$ includes contact forces $\mathbf{F}^c$ and friction forces $\mathbf{F}^r$. The Newton–Raphson method was used to find the root of $f(\mathbf{q}_{\text{new}}) = 0$ of Eq. 7, in which the Jacobian of Eq. (7) is defined as

$$\mathbf{J}_{ij} = \frac{m_i}{\Delta t^2}\delta_{ij} + \frac{\partial^2(E_s + E_b + E_t)}{\partial \mathbf{q}_i \partial \mathbf{q}_j} - \mathbf{J}_{ij}^c - \mathbf{J}_{ij}^r \tag{9}$$

where m_i is the mass of ith node, δ_{ij} is the Kronecker delta ($\delta_{ij} = 1$ when $i = j$, and $\delta_{ij} = 0$ when $i \neq j$), $\mathbf{J}_{ij}^c$ is the Jacobian of contact forces, and $\mathbf{J}_{ij}^r$ is the Jacobian of friction forces. The Jacobian of elastic energies can be obtained with Eqs. (2)–(4). More details of frictional contact forces $\mathbf{F}^c$ and $\mathbf{F}^r$ and their Jacobians $\mathbf{J}^c$ and $\mathbf{J}^r$ can be found in Ref. [9].

In addition to the elastic energies in DER formulation, contact and friction forces are also critical for simulating overhand knots. The contact energy and force model in Ref. [9] was adopted in this study, which is a penalty energy-based method. In this frictional

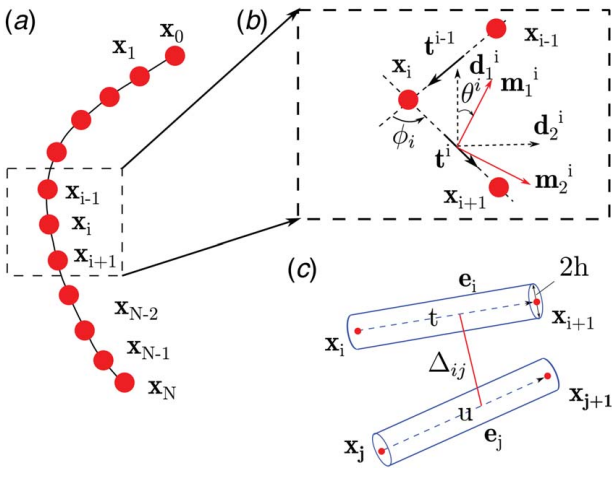

Fig. 2 Discrete schematic and relevant notations: (*a*) discrete schematic of an elastic rod, (*b*) discrete notations about the reference frame $[\mathbf{t}^i, \mathbf{d}_1^i, \mathbf{d}_2^i]$, the material frame $[\mathbf{t}^i, \mathbf{m}_1^i, \mathbf{m}_2^i]$, the twist angle θ^i, and the turning angle ϕ_i, and (c) schematic diagram of a contact pair including the edge $\mathbf{e}_i$ and $\mathbf{e}_j$

contact, frictional contact is regarded as a constraint by introducing penalty energy when solving the EOM.

A contact pair is defined by combining two edges $\mathbf{e}_i$ and $\mathbf{e}_j$, shown in Fig. 2(*c*), which is made up of nodes $\mathbf{x}_i$, $\mathbf{x}_{i+1}$, $\mathbf{x}_j$, and $\mathbf{x}_{j+1}$. Therefore, a contact pair can be denoted as the following vector concatenation, $\mathbf{x}_{ij} := (\mathbf{x}_i, \mathbf{x}_{i+1}, \mathbf{x}_j, \mathbf{x}_{j+1})$ (size 12×1). The formulation of the contact energy from Ref. [9] is written as

$$E(\mathbf{x}_{ij}) = \frac{\log\left(1 + \exp\left(ce_k(2h - \Delta_{ij})\right)\right)}{ce_k} \tag{10}$$

where ce_k is the contact stiffness—a user-defined parameter—which can determine the magnitude of the contact forces, and h is the radius of the rod.

The advantages of the above formulation of contact modeling are (1) the penetration between edges is avoided by introducing artificial penalty energy as a constraint. (2) Different from the Lumelsky algorithm [47], where the artificial energy is treated as a piecewise function, a smooth function is used to approximate the contact energy. Therefore, contact forces $\mathbf{F}_{ij}^c$ can be obtained via the negative gradient of the contact energy as $\mathbf{F}_{ij}^c = -\nabla E(\mathbf{x}_{ij})$, and the Jacobian $\mathbf{J}_{ij}^c$ can be obtained via the negative hessian of the contact energy through chain rules.

From Coulomb's friction, magnitude of friction forces is irrelevant with the relative velocity between edges $\mathbf{e}_i$ and $\mathbf{e}_j$. When sliding between two edges happens, the magnitude of friction force is $\|\mathbf{F}^{fr}\| = \mu\|\mathbf{F}^n\|$, where μ is the friction coefficient and $\mathbf{F}^n$ is the normal force. As mentioned before, the normal forces between edges $\mathbf{e}_i$ and $\mathbf{e}_j$ are $\mathbf{F}_{ij}^c = -\nabla E(\mathbf{x}_{ij})$. Therefore, we can define the normal contact force which is $\mathbf{F}^n = \mathbf{F}_i^c + \mathbf{F}_j^c$. The contact normal can also be calculated simply through $\mathbf{n} = \mathbf{F}^n/\|\mathbf{F}^n\|$. The direction of friction $\mathbf{F}^{fr}$ is then determined by tangential component of the relative velocity $(\mathbf{v}^{\text{rel}})^T$. For simplicity, we approximate the relative velocity as the relative velocity between the middle points of two edges.

$$\begin{aligned} \mathbf{v}^{\text{rel}} &= 0.5(\mathbf{v}_i + \mathbf{v}_{i+1}) - 0.5(\mathbf{v}_j + \mathbf{v}_{j+1}) \\ (\mathbf{v}^{\text{rel}})^T &= \mathbf{v}^{\text{rel}} - (\mathbf{v}^{\text{rel}} \cdot \mathbf{n})\mathbf{n} \\ (\hat{\mathbf{v}}^{\text{rel}})^T &= \frac{(\mathbf{v}^{\text{rel}})^T}{\|(\mathbf{v}^{\text{rel}})^T\|} \end{aligned} \tag{11}$$

wherein $\mathbf{v}_i$ and $\mathbf{v}_j$ are nodal velocities.

With Eq. (11), we determine the direction of the frictional forces. In order to simulate the static frictional forces, we introduce a weight $\gamma \in [0, 1]$, which will adjust the magnitude of frictional forces based on the sliding (tangential components of relative velocity): when γ is close to 1, the friction formulation will be the sliding friction; when γ is not close to 1, the sliding between the contacted segments should be small enough to simulate the static phenomena. Note that the frictional responses cannot be larger than $\mu\|F^n\|$.

$$\begin{aligned} \gamma &= \frac{1}{1 + \exp\left(-k(\|(\mathbf{v}^{\text{rel}})^T\| - c)\right)} \\ \mathbf{F}^{fr} &= -\gamma(\hat{\mathbf{v}}^{\text{rel}})^T \mu\|F^n\| \\ \mathbf{F}_{ij}^{fr} &= (0.5\mathbf{F}^{fr}, 0.5\mathbf{F}^{fr}, -0.5\mathbf{F}^{fr}, -0.5\mathbf{F}^{fr}) \end{aligned} \tag{12}$$

Note that k and c are hyperparameters that users can adjust. The definition of c is described before, and c states the limit for the step transition. During the simulation, we set all k as $50/r_0$ and c as $0.15r_0$. Under such parameters, γ will be close to 1 when the magnitude of the relative velocity is larger than 0.205 mm/s. In other words, when $\|v^{\text{rel}}\| > 0.205$ mm/s, the dominant friction forces will be sliding friction. $\mathbf{F}_{ij}^{fr}$ is a 12×1 force vector that can be added to discrete nodes of the rod, and its Jacobian $\mathbf{J}_{ij}^{fr}$ can be calculated with the chain rule as well. More details are available in Ref. [9].

The pulling force measured in the experiment is treated as an external force at the boundary in DER simulation to determine the friction coefficient.

3 Experimental Setup: Materials and Method

This section includes the materials used for the experiments and the method of the experiments. First, the preparation of the rods and the coating mixture is discussed. The following sections discuss the development of coating setup, characterization of the coated rod, and friction test method.

3.1 Preparation of Rods and Coating Mixture. Natural rubber rod (weather and abrasion-resistant; color: black; purchased from McMaster-Carr, USA) is used as the substrate to observe the variation of friction forces with the variation of particle volume fraction in the suspension. The temperature range of the rubber rod is −59 °C to 122 °C and the diameter (d) of the rod used in all the experiments is 1/16 in. (1.59 mm approximately). The Young's modulus (E) of the elastic rod is 1.83 MPa, measured by the universal testing machine (MTS criterion, USA) and the tensile strength of the rod is 17.24 MPa (manufacturer provided). The surface of the rod is fairly smooth and the friction will be introduced by delivering inorganic particle asperities on the surface. For uniform deposition of the particles on the rod substrate, a liquid carrier system (LCS) is prepared as the particle-bearing liquid.

The LCS consists of polymethyl methacrylate (MW ∼ 15000 g/mol; Sigma Aldrich, USA) as the binder, which has low density (∼1.19 g/cm^3), ∼41 mN/m surface tension, and is a benign, non-explosive, and non-flammable material [48]. 1,3-Dioxolane (from Sigma Aldrich, USA) is used as the solvent, which has 34.3 mN/m surface tension, 1.06 g/cm^3 density, and vapor pressure of 79 mmHg at 20 °C [49]. A magnetic stirrer is used for 8 h to confirm the complete dissolution of the granular solute in the liquid solvent, which is also confirmed by XPS (Fig. 3(*a*)). Iron metal reduced powder (particles size 45–150 μm, ChemCenter LLC, CA) is considered to create the asperities on the elastic rod surface. The solid inorganic particles are added at a premeasured particle volume fraction (ϕ_p) in the LCS gradually to create the dipping mixture as shown in Fig. 3(*b*).

Adding binder and immiscible particles to a liquid transforms its rheological properties. The addition of particles will act as obstacles to the fluid flow which will induce a non-linear dependency under applied shear (non-Newtonian). At a higher volume fraction, the mixture may exhibit friction-induced continuous shear thickening or discontinuous shear thickening [50], causing a stress-induced solid-like shear jammed state. Similarly, adding binder will increase the viscosity, which may facilitate the particle adherence, but it may cause non-uniform particle transfer due to the high viscosity nature of the mixture. For our experiments, the binder volume fraction is kept at $\phi_b = 5\%$, while the volume fraction of the particles is varied between $\phi_p = 1\%$ and 13% so that the mixture perform way below the effective viscous regime. The non-spherical irregular edged shape rough surface morphology of the raw particles is shown in Fig. 4. The particle size selected to alter the friction coefficient is ≪1 mm, which will ensure that the other relevant physical parameters (e.g., cross-sectional radius) are not altered when the friction is varied.

3.2 Development of Coating Setup. A standardized continuous dip coating protocol has been developed in our laboratory for depositing particles from a liquid carrier system to the cylindrical elastic rod substrate. The schematic of the coating setup is depicted in Fig. 5 which is composed of a dipping jar, guiding rollers, impeller, motor, and the control box for the motor. The dipping jar used in the experiments is cylindrical in shape, screw top, clear borosilicate glass with round bottom, and the inner diameter (D_i) and height of the dipping jar (H) are 80 mm and 100 mm, respectively. Two sink rollers ($R1$ and $R2$ in Fig. 5) are used as guides for the elastic rods to ensure the fixed dwelling time and another turn-up roller ($R3$) is used as a guide during the pulling of the coated rod by the motor M. The diameter of both $R1$ and $R2$ is 0.75 mm and the diameter of $R3$ is 35 mm. The gap between $R1$ and $R2$ (R) is 50 mm. The clearance between the two guide rollers ($R1$ and $R2$) and the impeller is 5 mm. The height of the mixture (Z) is kept at 60 mm, shown in Fig. 5.

The density of the particles is 7.8 g/cm^3 which is much higher than the LCS used in this experiment. Due to higher density, sedimentation of the particles is observed within a very short time. As a result, external kinetic energy is required to keep the particles suspended. A straight blade impeller is used in the experiments to provide kinetic energy to keep the particles suspended. The length (L) and the width (W) of the impeller are 70 mm and 12.5 mm, respectively, which are shown in Fig. 5. A pressure difference is created from the rotation of the impeller which helps the particles to encounter the gravitational force of the particles. The clearance between the impeller and the bottom of the dipping jar (C) is 5 mm. The rotational speed of the impeller is kept at just suspending speed of the particles to minimize the vortex in the mixture.

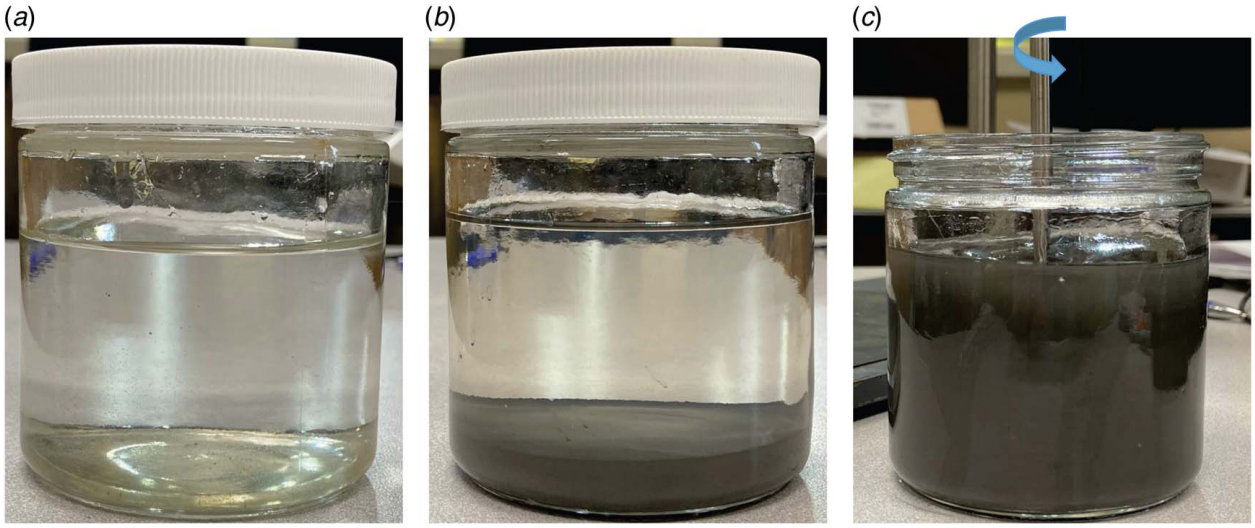

Fig. 3 Preparation of particle mixture: (*a*) LCS; solution (solute + solvent), (*b*) added particles in LCS, and (*c*) pseudo-suspension of the mixture by stirring

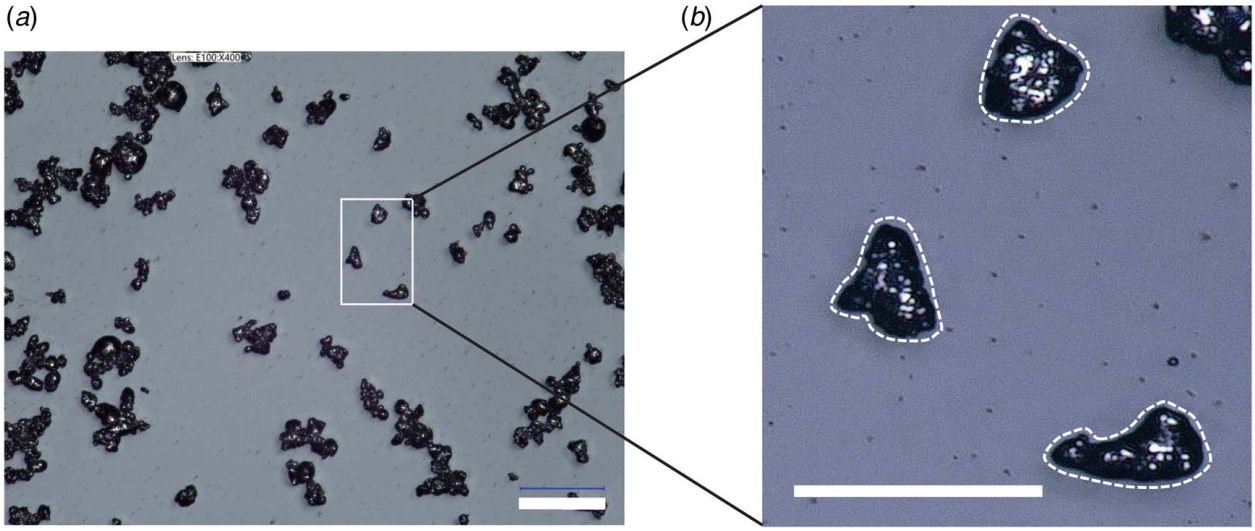

Fig. 4 (a) Shape and morphology of the raw particles. Scale bar is 100 μm for (a) and 50 μm for (b).

A Flashcut controller controls the motion of the motor, which is driven by G-code and pulls the rod. The withdrawal speed of the rod is kept at 5 mm/s which makes the dwell time of the rod in the suspension to be about 10 s. The withdrawal speed is controlled within $\pm 2\%$ precision by using the high-precision bipolar stepper motor (SANYO) connected to a computer. After the rod is immersed in the dipping mixture, the evaporating solvent dries from the surface before it reaches the roller $R3$, where C_R is 2.5 m. The coated rod is then collected and is placed inside an oven at 80 °C for an hour to ensure uniform drying.

3.3 Characterizing the Coated Rod. The morphology of the micro-particle-coated elastic rods is investigated after drying. VHX 7000 Digital 4K microscope (KEYENCE Corp., IL) at 400× is used for the imaging of the particle-coated elastic rods. High resolution

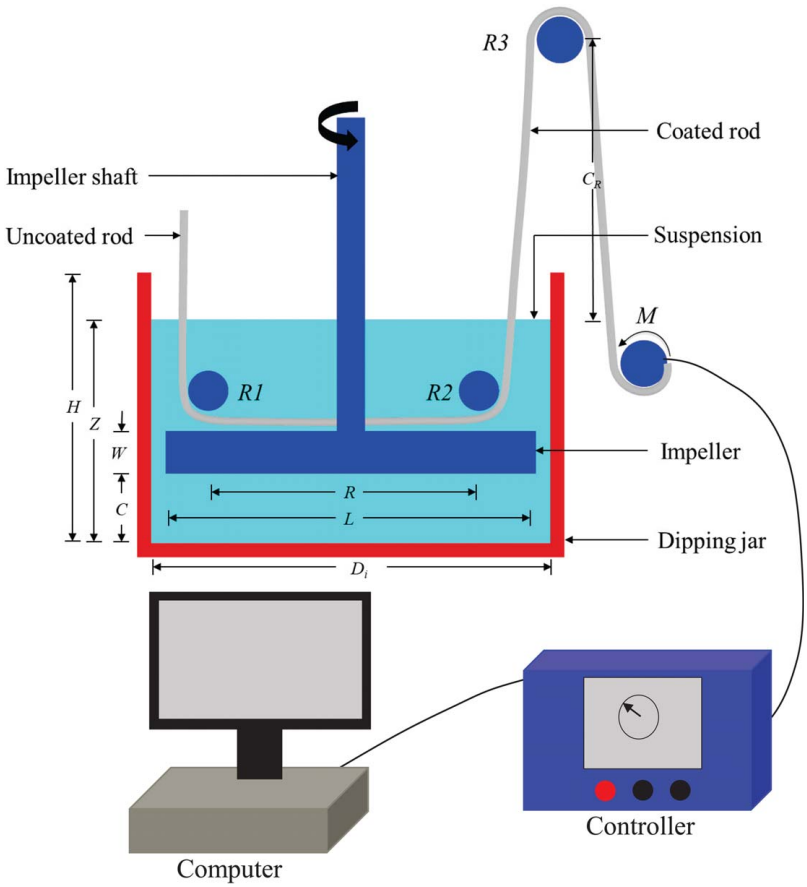

Fig. 5 Schematic diagram of the experimental setup for continuous coating of the elastic rod (not to scale)

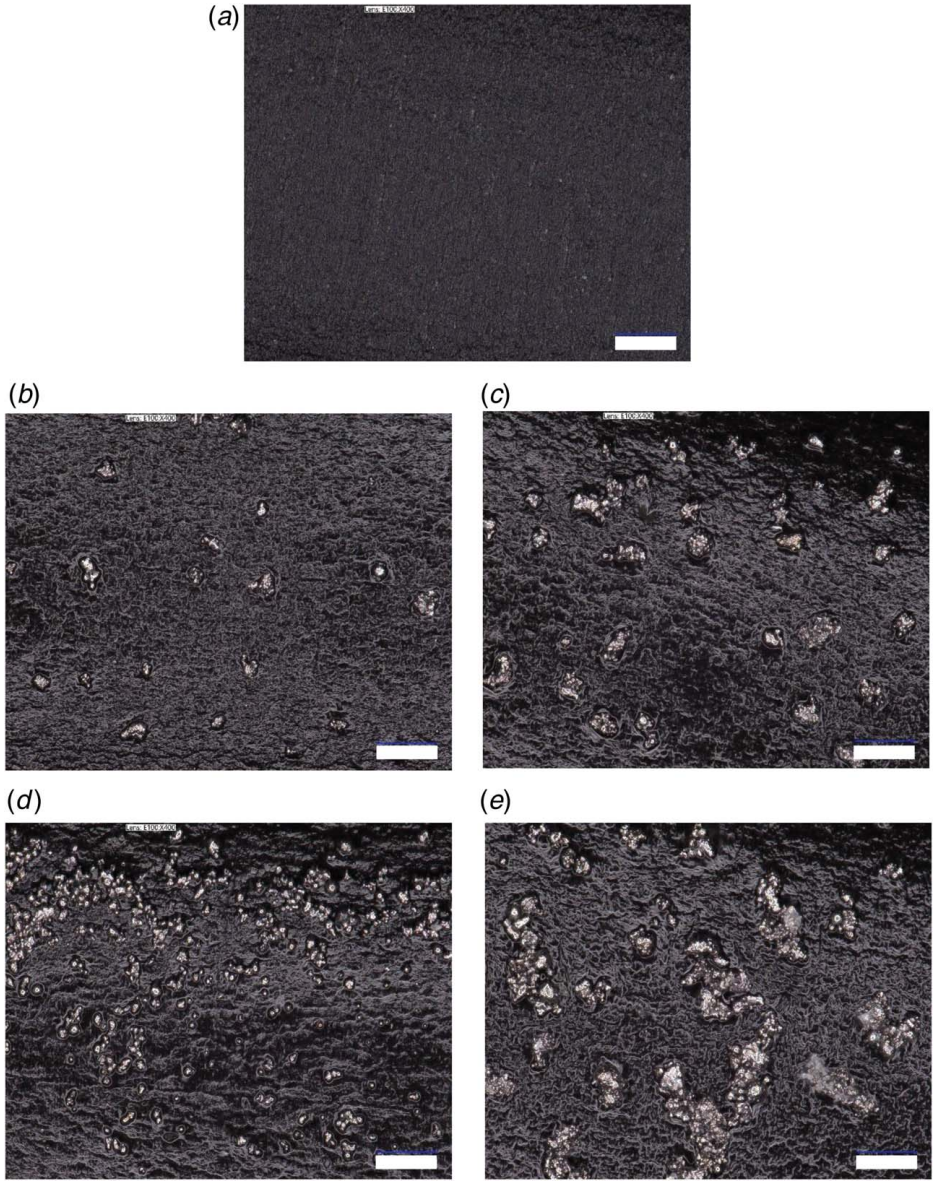

Fig. 6 Surface morphology of the elastic rod: (*a*) uncoated; coated with (*b*) 1% particle, (c) 4% particle, (*d*) 7% particle, and (e) 13% particle. Scale bar is 100 μm.

4K images of the dipped rod are taken with the microscope and the images are analyzed with IMAGEJ software. The surface morphology of the coated rod is shown in Fig. 6. Surface coverage is measured as the ratio of the area covered by the particles and the area of the rod. At least three images from three different regions are selected and analyzed over the substrate for determining the particle counts and surface coverage to ensure statistical significance. The variation of the coverage and particle count is presented in Fig. 7.

3.4 Developing the Friction Test Setup. To measure the friction, three samples of particle-coated elastic rods of 600 mm length are prepared and dried. Self-intersection of the rod is achieved by tying knots as shown in Fig. 8. One end of the coated rod is mounted to a fixed clamp and the other end is joined with the hook of the digital push–pull force gauge (20 N). The force gauge is connected to a computer and the variation of forces at different pulling lengths is recorded at a 10 Hz rate. The motion of the force gauge is controlled by a controller with high-precision

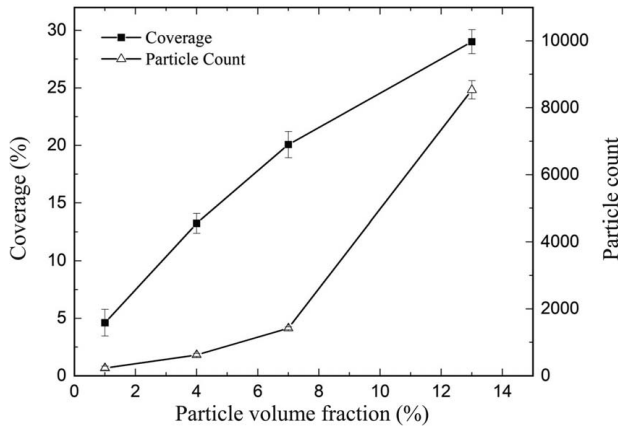

Fig. 7 Variation of coverage and particle count with particle volume fractions

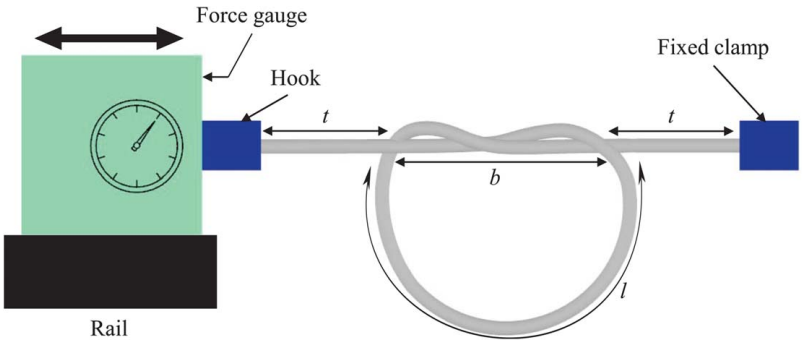

Fig. 8 Schematic diagram of pulling force measurement setup with different parameters of knots (not to scale)

bipolar stepper motor. The pulling speed of the rod is kept at 200 mm/min for the experiments.

In this present work, the length of self-intersection for the rod is controlled with knot numbers. Up to four knots are used to observe the variation of the friction force for the rod coated with different volume fraction of particles. Tail length (t), braid length (b), and loop arc length (l) are the defining parameters shown in Fig. 8. The end to end length is defined as the gap between the fixed clamp and hook of the force gauge where two ends of the elastic are mounted. Similar parameters can resemble the higher number of knots. The total length is taken as 300 mm for one and two knots, while 600 mm for three and four knots. This is to overcome the fluctuations of the forces due to the large tail length. Each friction test is performed three times to demonstrate the statistical significance. The parameters of different knots before pulling are listed in Table 1.

4 Results and Discussion

The experimental and simulation results are presented in this section. During the experiment, the forces required for pulling the rods are measured and discussed here. The asperities introduced by the adhesion of hard particles on the substrate are also discussed. The variation of forces measured by the push–pull force gauge is then plotted to compare with the simulation result in this section.

When the thin rod is dipped in the heterogeneous mixture, a thin polymer film is adsorbed at the solid–liquid interface, creating a viscous layer. As the rod exits the mixture, a convective flux acts on particles which is generated from the solvent evaporation and the capillary rise [28,51]. The upward convective flux increases with the withdrawal speed, and the viscous drag force starts to dominate the particle adhesion. At a lower volume fraction of binder and particles, the viscous layer is thinner and the capillary effect in LCS remains high. The balance between the viscous drag and the capillary action determines the particle entrainment on the rod substrate. Particle transfer occurs at the three-phase boundary [52] during the withdrawal stage due to entrainment, when the viscous drag force becomes larger than the resistive capillary force in liquid molecules. The liquid film thickness (viscous layer), particle size, and volume fraction influence the entrainment of particles [37]. The effects of convective flux acting on the particle-laden mixture vary due to particle polydispersity, which creates a variation in the viscous drag force for entrainment. Additionally, the volumetric density of particles in the entrainment zone can become higher than the rest of the mixture due to the continuous flux of particles formed by the convective forces in the heterogeneous mixture [51]. For this reason, entrained particle coverage can become higher than the corresponding particle area coverage in the bulk mixture which can be observed in Fig. 7. For example, with the same 10% volume fraction of particles in the mixture, coverage increases from 5% to 27%. The adhesion of these particles on the elastic rod transforms the smooth surface morphology through asperities.

During the pulling of the elastic rods, each strand of the braid is subjected to two external forces [3]. The forces are traction/pulling force (acting due to tensile load on the tails) and the friction forces (due to the self-contact of the rods in the braid). Total elastic energy of a rod is composed of stretching energy, twisting energy, and bending energy [9]. The detailed simulation process of the elastic rod is described in Sec. 2. The pulling force provided by the push–pull force gauge during the experiment can be used to determine the friction force and friction coefficient as discussed in Sec. 2.

The pulling force required is dependent on the surface asperities produced by the transferred particles adhered to the viscous binder layer, which can be observed in Figs. 9(*a*) and 9(*b*) representing the cross section of the uncoated and coated substrates. The polymer layer thickness is a function of dimensionless capillary number which is measured as ($5.85 \pm 0.17\ \mu$m) using a VHX 7000 Digital 4K microscope (KEYENCE corp., IL) after 8 h from dipping. During the continuous dipping process described in Sec. 3, particles are entrained on the viscous layer changing the surface morphology. We have observed some loss of loosely adhered particles during pulling, but the number is insignificant compared to the total number of transferred particles. The oven drying has helped the uniform adhesion of particles on the substrate and no significant

Table 1 Pulling parameters for different knots ($n = 1, 2, 3, 4$)

Knot (n)	Tail length, t (mm)	Braid length, b (mm)	Loop arc length, l (mm)	End to end length (mm)
1	35	30	170	100
2	25	55	140	100
3	80	95	250	250
4	45	110	290	200

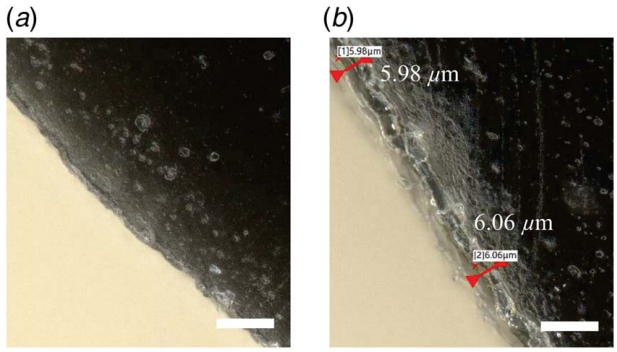

Fig. 9 Cross section of the elastic rod: (*a*) uncoated and (*b*) polymer coated. The polymer film is clearly evident in (*b*). Scale bar is 25 μm.

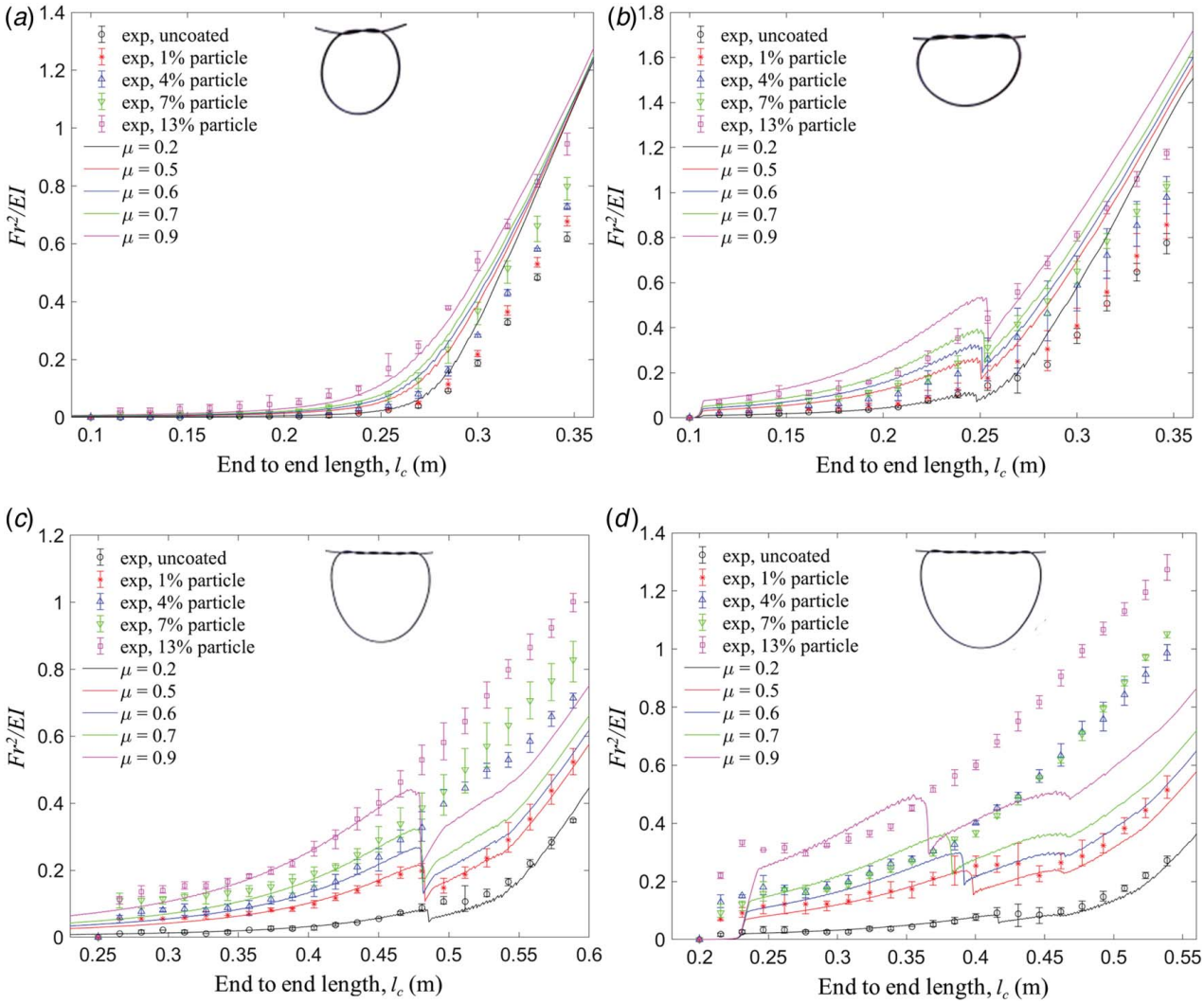

Fig. 10 Experimental and simulation result of pulling force: (*a*) one knot, (*b*) two knots, (c) three knots, and (*d*) four knots. The point with the error bar represents the experimental results and the continuous line represents the simulation results.

difference between the three pulling replications has been observed in our experiment. Increasing the particle volume fraction in the dipping mixture increases the volumetric density of particles in the entrainment zone and a systematic variation can be observed in Fig. 6.

The deposition of the particles on the elastic rod increases with the increase of the particle volume fraction in the suspension. Uniformly distributed particles deposition over the substrate is observed for lower volume fraction (≤7%) particle. Particles started to cluster at an increased volume fraction (13%) as shown in Fig. 6(*e*). Such aggregates will induce larger asperities, which can increase the self-intersecting friction during pulling. Surface coverage follows the similar pattern of increased coverage with increasing volume fraction as shown in Fig. 7. A total of 4.61 ± 1.15% surface coverage is measured for 1% particle volume fraction while the maximum surface coverage (29.02 ± 1.05%) is observed with the 13% particle volume fraction in the suspension. Particle count also follows the similar pattern as the surface coverage (i.e., minimum particle count is observed in 1% and maximum particle count is observed in 13% particle) which is presented in Fig. 7. The pulling forces recorded by the force gauge confirm this relationship of increasing friction forces.

The experimental results shown in Fig. 10 represent the increasing trend of pulling forces with increased particle volume fraction and contact area (i.e., knot number). Regularized pull force (Fr^2/EI) is plotted against end to end length (l_c), where F is the pull force, r is the cross-sectional radius of the rod, and EI is the bending stiffness. For each knot number, the contact area in the braid represented in the knot geometry (shown in Fig. 8) remains the same. Due to the thin polymer layer generation after coating, no significant difference can be assumed between coated and uncoated contact areas along the length. Furthermore, no infusion of polymer binder can be observed from the cross section (Fig. 9), thus the elastic properties of the rod before and after coating have been assumed unchanged in our simulation. As a result, the variation in the external pulling force within each knot can be attributed to the change in contact friction force. The uncoated rod experienced the lowest friction force at each end to end length which gradually increases with particle volume fraction. Three sets of data are collected for each experiment with each knot and particle volume fraction. The simulation data are generated and compared with best fitted friction coefficient parameter which is found as $\mu = 0.2, 0.5, 0.6, 0.7,$ and 0.9 for uncoated, 1%, 4%, 7%, and 13%, respectively. The fitting between simulation and experimental data can be observed in Fig. 11. We observed good agreement between simulation and experimental results with few exceptions, which is discussed in the later section.

Comparison of the experimental and the simulation results at different conditions are shown in Fig. 10 which demonstrates the increase in friction forces with the increase in knot number and

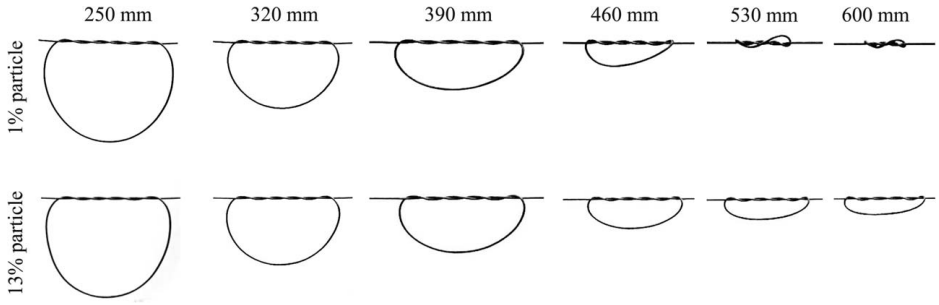

Fig. 11 Change in shape of knots ($n = 3$) rods coated with 1% (top) and 13% (bottom) particle

particle volume fraction. During pulling, a tensile force will be applied along the tail length which will propagate through the braid length. This will create a sliding motion shrinking the loop length. As a result, static friction followed by dynamic friction should be observed in our force–displacement plot. The higher slope at the beginning of the force–displacement curve represents the static friction; after that, dynamic friction shows gradual increase in the friction force. This is clearly observed for $n > 1$ in both experimental and simulation results. However, for $n = 1$, sudden increase of the friction force at the beginning of pulling (static friction) is not observed due to minimum contact area in the braid length.

During pulling of the tails, the traction/pulling force is transferred along the longitudinal direction of the rod. Due to the self-intersecting topology of the knot, an opposing friction force will act to counter the traction/pulling force. As the magnitude of the traction/pulling force increases, the internal energy of the rod (i.e., stretching, twisting, and bending) increases accordingly, which is expressed in Eq. (9). The spiral topology of the knots creates two opposing flows at the braid resulting in a local moment inside the loop. Additionally, it counters the global moment caused at the two ends of the tails due to pulling. The sliding force facilitates the internal moment causing instability in the loop which is defined as the inversion point [9]. A sudden drop in pull force can be observed at the inversion point and the knot comes to the lowest energy state. In experiments, when the sliding is refrained due to higher friction caused by asperities or contact area (knot number), the knot starts to behave differently and stretching energy dominates the pulling behavior. In such scenarios, no inversion point can be observed. In another word, inversion or no inversion will depend upon the friction force experienced at the knot. These phenomena are clearly evident in our experimental result presented in Fig. 10.

At single knot ($n = 1$), no inversion point can be observed in both experiment and simulation results. This is due to minimum self-contact sliding region which result in minimum friction force. The force versus displacement curve generated by experiment and simulation shows good agreement till the end to end length of 250 mm. Afterward, the simulation data overpredict the experimental results except 13% particle volume fraction. The overprediction by the simulation can be observed in two knots as well. However, inversion point has been observed for uncoated ($\mu = 0.2$) and 1% particle ($\mu = 0.5$) volume fraction. The drop in forces at the inversion point is relatively low compared to the prediction from simulation. For higher friction coefficient ($\mu = 0.6, 0.7,$ and 0.9), the deviation increases including disagreement in inversion point, but the curve shows similar pattern. It is observed both from the experiment and simulation that the inversion point occurs sooner as the friction increase. This shows the dependency of the inversion point with friction coefficient [9].

In case of three and four knots ($n = 3$ and 4), the experimental result nicely follows the prediction from simulation. The fits mostly remain within the one sigma of the error bar till the inversion points. Inversion point has been observed for uncoated ($\mu = 0.2$) and 1% particle ($\mu = 0.5$) volume fraction. Both the drop in force and the predicted force match the experiment beyond the inversion point. It should be noted that no inversion point can be observed for higher friction coefficient ($\mu = 0.6, 0.7,$ and 0.9) due to the complex nature of the acting force discussed above.

Variation in the shape of the knots, presented in Fig. 11, confirms the effect of the particle volume fractions on the friction forces. The snapshot of the knots is taken at six different positions for the uncoated rod and the coated with 13% particle in the suspension and is presented in this work. It is clearly evident from Fig. 11 that the shape of the knots at different pulling lengths is controlled by the friction coefficients of the coated rods that depends on the particle volume fractions in the suspensions.

The relation between the friction coefficient and the particle volume fraction is shown in Fig. 12 which shows that the variation of the coefficient of the friction is directly dictated by the volume fraction of particles in the suspension. It is observed from Fig. 12 that coated rod with only 1% particle in the suspension changes the friction coefficient almost 150% ($\mu = 0.5$). Moreover, proportional relationship is observed between the variation of friction coefficient and particle volume fraction in the suspension. To compare the fitted simulation, an experiment is designed to measure the friction coefficient following the capstan equation. A larger diameter rod (1/4 in.) of the same material is used as the capstan. Both the capstan and the rod are coated in the same suspension following the protocol discussed earlier. The rod slides over the capstan following the weight difference at two ends and the friction coefficient is calculated [53] which is presented in Fig. 6. The friction coefficient of the coated rod increases with the increase of the particle volume fraction in the suspension which is also observed in the simulation results. A slight variation between capstan and simulation method can be observed at higher particle volume fractions (7% and 13%). This is due to particle cluster formation at higher

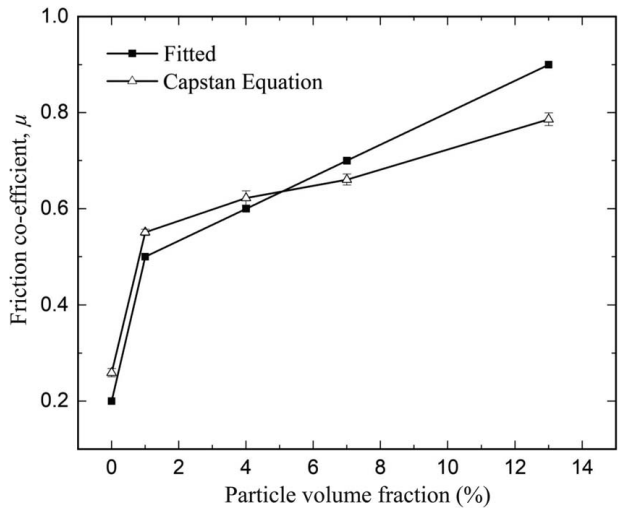

Fig. 12 Variation of friction coefficient with particle volume fractions

particle volume fractions compared to non-clustered particle distributed at low particle volume fraction (uncoated, 1%, and 4%) coat. The similar trend between the two methods demonstrates the accuracy of our proposed simulation technique. This relationship between the friction coefficient and particle volume fraction can help to predict the required particle volume fractions for achieving desired friction coefficient.

5 Concluding Remarks

This article reports a novel method for the variation of friction forces of the elastic rods by adhering non-spherical irregular edged shaped particles. When the particles are transferred, asperities are introduced over the surface which results in an increase in the friction forces. The particle transfer increases with the increase in the particle volume fraction in the suspension. The friction force increases during the self-contact of the rods due to the increase in particle transfer. Experimental results demonstrate the variation of friction forces and friction coefficient with particle volume fractions. Moreover, a systematic variation of experimental value of the friction force is observed with the particle volume fractions in the suspension except one case in four knots. The relationship between the friction coefficient and particle volume fraction in the suspension shows promising result to manufacture an elastic rod with specific friction coefficient. The results can be extrapolated to find the particle volume fraction to obtain an elastic rod with desired friction coefficient. However, change in particle morphology may require to establish a new relationship.

A numerical prediction technique is also proposed and implemented for determining the coefficient of friction which shows good agreement with the experiment data at lower coefficient of friction. Some disagreements can be observed with the increase in asperities due to the effect of the other forces (bending, twisting, and contact forces; the moment due to these forces) present at higher contact area (increased knot number) and higher friction force. Some possible causes of discrepancies in Fig. 11 may also be attributed to particle clustering, particle poldispersity, irregular particle shape, local variation in adhered particle distribution, and change in mechanical properties of the coated rod. Performing the experiment at a slow speed, with uniform particle morphology, and gripping the tail to avoid rotation can help minimize the difference between experiment and simulation results.

Acknowledgment

This research was funded by the National Science Foundation (Award # CMMI-2101751 and CMMI-2101745). M.K.J. and D.T. also acknowledge support from the National Science Foundation (Award # IIS-1925360).

Conflict of Interest

There are no conflicts of interest.

Data Availability Statement

The datasets generated and supporting the findings of this article are obtainable from the corresponding author upon reasonable request.

References

[1] Ashley, C. W., 1944, *The Ashley Book of Knots*, Doubleday Books, New York.
[2] Moulton, D. E., Grandgeorge, P., and Neukirch, S., 2018, "Stable Elastic Knots With No Self-contact," J. Mech. Phys. Solids, **116**, pp. 33–53.
[3] Jawed, M. K., Dieleman, P., Audoly, B., and Reis, P. M., 2015, "Untangling the Mechanics and Topology in the Frictional Response of Long Overhand Elastic Knots," Phys. Rev. Lett., **115**(11), p. 118302.
[4] Patil, V. P., Kos, Z., Ravnik, M., and Dunkel, J., 2020, "Discharging Dynamics of Topological Batteries," Phys. Rev. Res., **2**(4), p. 043196.
[5] Clauvelin, N., Audoly, B., and Neukirch, S., 2009, "Matched Asymptotic Expansions for Twisted Elastic Knots: A Self-contact Problem With Non-trivial Contact Topology," J. Mech. Phys. Solids, **57**(9), pp. 1623–1656.
[6] Daviet, G., Bertails-Descoubes, F., and Boissieux, L., 2011, "A Hybrid Iterative Solver for Robustly Capturing Coulomb Friction in Hair Dynamics," Proceedings of the 2011 SIGGRAPH Asia Conference, Hong Kong, Dec. 12–15, pp. 1–12.
[7] Durville, D., 2012, "Contact-Friction Modeling Within Elastic Beam Assemblies: An Application to Knot Tightening," Comput. Mech., **49**(6), pp. 687–707.
[8] Kaufman, D. M., Tamstorf, R., Smith, B., Aubry, J.-M., and Grinspun, E., 2014, "Adaptive Nonlinearity for Collisions in Complex Rod Assemblies," ACM Trans. Graph., **33**(4), pp. 1–12.
[9] Choi, A., Tong, D., Jawed, M. K., and Joo, J., 2021, "Implicit Contact Model for Discrete Elastic Rods in Knot Tying," ASME J. Appl. Mech., **88**(5), p. 051010.
[10] Li, M., Ferguson, Z., Schneider, T., Langlois, T., Zorin, D., Panozzo, D., Jiang, C., and Kaufman, D. M., 2020, "Incremental Potential Contact: Intersection- and Inversion-Free, Large-Deformation Dynamics," ACM Trans. Graph., **39**(4), pp. 49:1–49:20.
[11] Patil, V. P., Sandt, J. D., Kolle, M., and Dunkel, J., 2020, "Topological Mechanics of Knots and Tangles," Science, **367**(6473), pp. 71–75.
[12] Kang, D. W., Kang, M., and Hahn, J. W., 2015, "Keystone Error Analysis of Projection Optics in a Maskless Lithography System," Int. J. Precis. Eng. Manuf., **16**(2), pp. 373–378.
[13] Lv, J.-T., Yan, Y., Zhang, W.-K., Liu, Y.-H., Jiang, Z.-Y., and Si, G.-Y., 2015, "Plasmonic Nanoantennae Fabricated by Focused Ion Beam Milling," Int. J. Precis. Eng. Manuf., **16**(4), pp. 851–855.
[14] Kobayashi, T., Bando, M., Kimura, N., Shimizu, K., Kadono, K., Umezu, N., Miyahara, K., Hayazaki, S., Nagai, S., Mizuguchi, Y., and Murakami, Y., 2013, "Production of a 100-m-Long High-Quality Graphene Transparent Conductive Film by Roll-to-Roll Chemical Vapor Deposition and Transfer Process," Appl. Phys. Lett., **102**(2), p. 023112.
[15] Chu, W.-S., Kim, C.-S., Lee, H.-T., Choi, J.-O., Park, J.-I., Song, J.-H., Jang, K.-H., and Ahn, S.-H., 2014, "Hybrid Manufacturing in Micro/Nano Scale: A Review," Int. J. Precis. Eng. Manuf. Green Technol., **1**(1), pp. 75–92.
[16] Hong, Y.-S., Lee, S.-R., Kim, J.-H., and Lee, S.-Y., 2015, "Application of a DLC-Coating for Improving Hydrostatic Piston Shoe Bearing Performance Under Mixed Friction Conditions," Int. J. Precis. Eng. Manuf., **16**(2), pp. 335–341.
[17] Yang, Y., Kim, K.-H., and Ong, J. L., 2005, "A Review on Calcium Phosphate Coatings Produced Using a Sputtering Process—An Alternative to Plasma Spraying," Biomaterials, **26**(3), pp. 327–337.
[18] Han, S. C., Choi, J. M., Liu, G., and Kang, K., 2017, "A Microscopic Shell Structure With Schwarz's D-Surface," Sci. Rep., **7**(1), pp. 1–8.
[19] Brinker, C., Frye, G., Hurd, A., and Ashley, C., 1991, "Fundamentals of Sol–Gel Dip Coating," Thin Solid Films, **201**(1), pp. 97–108.
[20] Hench, L. L., and West, J. K., 1990, "The Sol–Gel Process," Chem. Rev., **90**(1), pp. 33–72.
[21] Xiao, Y., Xu, Z., Liu, Y., Peng, L., Xi, J., Fang, B., Guo, F., Li, P., and Gao, C., 2017, "Sheet Collapsing Approach for Rubber-Like Graphene Papers," ACS Nano, **11**(8), pp. 8092–8102.
[22] Park, J., Shin, K., and Lee, C., 2014, "Optimized Design for Anti-reflection Coating Process in Roll-to-Roll Slot-Die Coating System," Rob. Comput. Integr. Manuf., **30**(5), pp. 432–441.
[23] Ressel, J., Seewald, O., Bremser, W., Reicher, H.-P., and Strube, O. I., 2018, "Low Friction Poly (Amide-Imide) Coatings With Silicones as Tethered Liquids," Prog. Org. Coat., **124**, pp. 1–7.
[24] Iijima, M., Muguruma, T., Brantley, W., Choe, H.-C., Nakagaki, S., Alapati, S. B., and Mizoguchi, I., 2012, "Effect of Coating on Properties of Esthetic Orthodontic Nickel–Titanium Wires," Angle Orthod., **82**(2), pp. 319–325.
[25] Kikuchi, Y., Graves, V. B., Strother, C. M., McDermott, J. C., Babel, S. G., and Crummy, A. B., 1989, "A New Guidewire With Kink-Resistant Core and Low-Friction Coating," Cardiovasc. Interv. Radiol., **12**(2), pp. 107–109.
[26] Murray, T. J., 2008, "Poly (Amide-Imides): Wire Enamels With Excellent Thermal and Chemical Properties," Macromol. Mater. Eng., **293**(5), pp. 350–360.
[27] Holmberg, K., 1992, "A Concept for Friction Mechanisms of Coated Surfaces," Surf. Coat. Technol., **56**(1), pp. 1–10.
[28] Khoda, B., Ahsan, A., and Shovon, S., 2021, "Dip Coating From Density Mismatching Mixture," J. Micro Nano-Manuf., **9**(2), p. 021003.
[29] Khoda, B., Nazmul Ahsan, A., and Shovon, S. N., 2021, "Solid Transfer of Large Particles by Dipping in a Heterogeneous Mixture," International Manufacturing Science and Engineering Conference, Virtual Online, June 21–25, Vol. 85079, American Society of Mechanical Engineers, p. V002T08A017.
[30] Rio, E., and Boulogne, F., 2017, "Withdrawing a Solid From a Bath: How Much Liquid Is Coated?," Adv. Colloid Interface Sci., **247**, pp. 100–114.
[31] Levich, B., and Landau, L., 1988, "Dragging of a Liquid by a Moving Plate," *Dynamics of Curved Fronts*, P. Pelce, ed., Academic Press, San Diego, CA, pp. 141–153.
[32] Deryagin, B., and Titievskaya, A., 1945, "Experimental Study of Liquid Film Thickness Left on a Solid Wall After Receeding Meniscus," Dokl. Akad. Nauk USSR, **50**, pp. 307–310.
[33] White, D. A., and Tallmadge, J. A., 1966, "A Theory of Withdrawal of Cylinders From Liquid Baths," AIChE J., **12**(2), pp. 333–339.
[34] Islam, C., and Altintas, Y., 2019, "A Two-Dimensional Transient Thermal Model for Coated Cutting Tools," ASME J. Manuf. Sci. Eng., **141**(7), p. 071003.
[35] Galio, A., Lamaka, S., Zheludkevich, M., Dick, L., Müller, I., and Ferreira, M., 2010, "Inhibitor-Doped Sol–Gel Coatings for Corrosion Protection of Magnesium Alloy AZ31," Surf. Coat. Technol., **204**(9–10), pp. 1479–1486.

[36] Crosley, M. S., and Yip, W. T., 2018, "Kinetically Doped Silica Sol–Gel Optical Biosensors: Expanding Potential Through Dip-Coating," ACS Omega, **3**(7), pp. 7971–7978.
[37] Khalil, I., and Khoda, B., 2022, "Sorting of Poly-Disperse Particle by Entrapment Using Liquid Carrier System," ASME J. Manuf. Sci. Eng., **144**(5), p. 054502.
[38] Dincau, B., Bazant, M., Dressaire, E., and Sauret, A., 2019, "Capillary Sorting of Particles by Dip Coating," Phys. Rev. Appl., **12**(1), p. 011001.
[39] Khoda, B., and Ahsan, A. N., 2021, "A Novel Rapid Manufacturing Process for Metal Lattice Structure," 3D Print. Additive Manuf., **8**(2), pp. 111–125.
[40] Khoda, B., Ahsan, A., Shovon, A. N., and Alam, A. I., 2021, "3d Metal Lattice Structure Manufacturing With Continuous Rods," Sci. Rep., **11**(1), pp. 1–17.
[41] Bergou, M., Wardetzky, M., Robinson, S., Audoly, B., and Grinspun, E., 2008, "Discrete Elastic Rods," ACM Trans. Graph., **27**(3), p. 63.
[42] Bergou, M., Audoly, B., Vouga, E., Wardetzky, M., and Grinspun, E., 2010, "Discrete Viscous Threads," ACM Trans. Graph., **29**(4), p. 116.
[43] Jawed, M. K., Novelia, A., and O'Reilly, O. M., 2018, *A Primer on the Kinematics of Discrete Elastic Rods*, Springer, Cham, Switzerland.
[44] Jawed, M. K., Da, F., Joo, J., Grinspun, E., and Reis, P. M., 2014, "Coiling of Elastic Rods on Rigid Substrates," Proc. Natl. Acad. Sci. U.S.A., **111**(41), pp. 14663–14668.
[45] Jawed, M. K., Khouri, N. K., Da, F., Grinspun, E., and Reis, P. M., 2015, "Propulsion and Instability of a Flexible Helical Rod Rotating in a Viscous Fluid," Phys. Rev. Lett., **115**(16), p. 168101.
[46] Baek, C., Sageman-Furnas, A. O., Jawed, M. K., and Reis, P. M., 2018, "Form Finding in Elastic Gridshells," Proc. Natl. Acad. Sci. U.S.A., **115**(1), pp. 75–80.
[47] Lumelsky, V. J., 1985, "On Fast Computation of Distance Between Line Segments," Inf. Process. Lett., **21**(2), pp. 55–61.
[48] Ali, U., Karim, K. J. B. A., and Buang, N. A., 2015, "A Review of the Properties and Applications of Poly (Methyl Methacrylate) (PMMA)," Polym. Rev., **55**(4), pp. 678–705.
[49] Riddick, J., Bunger, W., and Sakano, T., 1985, *Techniques of Chemistry, Organic Solvents*, Vol. 2, John Wiley and Sons, New York.
[50] Dhar, S., Chattopadhyay, S., and Majumdar, S., 2019, "Signature of Jamming Under Steady Shear in Dense Particulate Suspensions," J. Phys.: Condens. Matter, **32**(12), p. 124002.
[51] Shovon, S., Alam, A., Gramlich, W., and Khoda, B., 2022, "Micro-particle Entrainment From Density Mismatched Liquid Carrier System," Sci. Rep., **12**(1), pp. 1–13.
[52] Prevo, B. G., Kuncicky, D. M., and Velev, O. D., 2007, "Engineered Deposition of Coatings From Nano- and Micro-particles: A Brief Review of Convective Assembly at High Volume Fraction," Colloids Surf. A, **311**(1–3), pp. 2–10.
[53] Sinclair, M., Ofek, E., Gonzalez-Franco, M., and Holz, C., 2019, "Capstancrunch: A Haptic VR Controller With User-Supplied Force Feedback," Proceedings of the 32nd Annual ACM Symposium on User Interface Software and Technology, New Orleans, LA, Oct. 20–23, pp. 815–829.